Journal of Alloys and Compounds 555 (2013) 184–192

Contents lists available at SciVerse ScienceDirect

Journal of Alloys and Compounds

journal homepage: www.elsevier.com/locate/jalcom

Experimental investigation of the $3Tl_2Se + Sb_2Te_3 \leftrightarrow 3Tl_2Te + Sb_2Se_3$ phase diagram

Yasin I. Jafarov [a], Mahammad B. Babanly [a,*], Andrei V. Shevelkov [b,*], Ziya S. Aliev [a]

[a] Baku State University, General and Inorganic Chemistry Department, Azerbaijan
[b] Moscow Lomonosov State University, Chemistry Department, Russia

ARTICLE INFO

Article history:
Received 18 September 2012
Received in revised form 26 November 2012
Accepted 30 November 2012
Available online 21 December 2012

Keywords:
Quaternary system
Thallium selenide
Antimony telluride
Phase diagram
Thermodynamic properties
Electro-motive force

ABSTRACT

Phase equilibriums were established in the $3Tl_2Se + Sb_2Te_3 \leftrightarrow 3Tl_2Te + Sb_2Se_3$ mutual system mainly by the X-ray powder diffraction and differential thermal analyses, with the aid of microhardness and EMF measurements applied to equilibrated alloys. According to the obtained experimental results the phase diagrams in form of the polythermal section and isothermal section at 300 K as well as the projection of the liquids surface have been constructed. It was found experimentally that the system is mutually reversible and is characterized by a wide solid solubility fields along the $TlSbSe_2$–$TlSbTe_2$ subsystem and within the Tl_2Se–Tl_9SbSe_6–Tl_9SbTe_6–Tl_2Te subsystem. The homogeneity and primary crystallization fields as well as the types and coordinates of non- and monovariant equilibriums were determined. The dependencies of crystallographic parameters, microhardness and EMF values upon the composition are discussed. From the EMF measurements, the partial molar functions of thallium ($\Delta\overline{G}, \Delta\overline{H}, \Delta\overline{S}$) were calculated for the revealed nonstoichiometric quaternary phases.

1. Introduction

Complex chalcogenides of heavy *p* metals exhibit properties that make them a good base for creating various functional materials, including thermoelectrics [1–3] and three-dimensional (3D) topological insulators [4,5]. These properties open the opportunity to realize a number of new applications in thermoelectrics, spintronics and quantum computing.

In recent years, phase diagrams of several ternary and quaternary systems consisting of chalcogenides of thallium, antimony and bismuth have been investigated. These systems include Tl_2S–Sb_2S_3–Bi_2S_3 [6], Tl_2Se–Sb_2Se_3–Bi_2Se_3 [7], Tl_2Te–Sb_2Te_3–Bi_2Te_3 [8], $3Tl_2S + Sb_2Se_3 \leftrightarrow 3Tl_2Se + Sb_2S_3$ [9], $3Tl_2S + Bi_2Se_3 \leftrightarrow Tl_2Se + Bi_2S_3$ [10], $3Tl_2S + Bi_2Te_3 \leftrightarrow 3Tl_2Te + Bi_2S_3$ [11] and $3Tl_2Te + Bi_2Se_3 \leftrightarrow 3Tl_2Se + Bi_2Te_3$ [12]. In these systems, new quaternary phases with sizable homogeneity ranges were found and subsequently studied for their physicochemical properties.

Understanding the phase relationships in the corresponding systems is always helpful for the development of relative materials. Specifically, the synthesis and growth of the large single crystals from the melt requires the knowledge of the respective phase diagrams. Quaternary phases are much more complex than ternary ones; at the same time they frequently contain quaternary analogs of known ternary phases but with complex substitutional patterns and wide homogeneity ranges. In many cases these phases represent certain interest as objects for varying and tuning properties of their parent compounds.

Here, we report the results of the complete investigation of phase equilibriums in the $3Tl_2Se + Sb_2Te_3 \leftrightarrow 3Tl_2Te + Sb_2Se_3$ quaternary mutual system hereafter denoted (A). We open this paper with reviewing the necessary literature data on the border systems and compounds in them, follow with the experimental procedure, and then discuss our data on the phase equilibriums, polythermal sections, liquidus surface, and partial molar thermodynamic functions.

1.1. Binary compounds

Initial binary compounds Tl_2Se, Tl_2Te, Sb_2Se_3 and Sb_2Te_3 forming the $3Tl_2Se + Sb_2Te_3 \leftrightarrow 3Tl_2Te + Sb_2Se_3$ quaternary mutual system all melt congruently at 663, 698, 863 and 895 K, respectively [13,14]. Tl_2Se crystallizes in the tetragonal system, space group $P4/n$, $a = 8.54$, $c = 12.71$ Å, $z = 10$ [15], whereas Tl_2Te forms the monoclinic lattice with the following unit cell parameters: $a = 15.662$, $b = 8.987$, $c = 31.196$ Å, $\beta = 100.761°$, $z = 44$ and the space group $C2/c$ [16]. Sb_2Se_3 has the orthorhombic crystal structure, space group $Pbnm$: $a = 11.633$; $b = 11.780$; $c = 3.985$ Å; $z = 4$, whereas Sb_2Te_3 crystallizes in the rhombohedral tetradymite type of structure with the unit cell parameters: $a = 4.25$; $c = 30.2$ Å, $z = 9$ [15].

* Corresponding authors. Addresses: Z. Khalilov Str. 23, Baku, AZ 1148, Azerbaijan (M.B. Babanly), Leninskie Gory 1-3, Moscow 119991, Russia (A.V. Shevelkov).

E-mail addresses: babanly_mb@rambler.ru (M.B. Babanly), shev@inorg.chem.msu.ru (A.V. Shevelkov).

0925-8388/$ - see front matter © 2012 Elsevier B.V. All rights reserved.
http://dx.doi.org/10.1016/j.jallcom.2012.11.202

1.2. Quasi-binary border subsystems and ternary compounds

1.2.1. The section Tl_2Se–Tl_2Te

This quasi-binary section relates to the eutectic type with the limited solid solubility fields based on the initial compounds. The eutectic composition lies at 20 mol% Tl_2Te and 648 K [17].

1.2.2. The section Tl_2Se–Sb_2Se_3

In our previous work [18], the refined phase diagram of this system was reported. Four ternary compounds, namely Tl_9SbSe_6, Tl_3SbSe_3, $TlSbSe_2$ and $TlSb_3Se_5$ were confirmed in this system. Two of them Tl_9SbSe_6 and $TlSbSe_2$ melt congruently at 725 and 730 K, respectively, whereas Tl_3SbSe_3 and $TlSb_3Se_5$ are formed by peritectic reactions at 625 and 740 K, respectively. The compositions of the peritectic points lie at 26 and 70 mol% Sb_2Se_3, respectively. The eutectic composition between $TlSbSe_2$ and Tl_3SbSe_3 has the melting point of 610 K at 28 mol% Sb_2Se_3, whereas the eutectic composition formed by $TlSb_3Se_5$ and $TlSbSe_2$ crystallizes at 705 K and 64 mol% Sb_2Se_3.

$TlSbSe_2$ undergoes a phase transition at 665 K. The low temperature modification crystallizes in the monoclinic system, space group $P2_1$ with the following unit cell parameters: $a = 9.137$, $b = 4.097$, $c = 12.765$ Å, $\beta = 111.75°$ [19], whereas the high temperature modification has the orthorhombic crystal structure with the unit cell parameters $a = 9.138$; $b = 23.735$; $c = 4.107$ Å [20]; it presents a disordered variant of the TlI structure type. Olsen and coauthors [21] reported that Tl_3SbSe_3 crystallizes in the Na_3AsS_3-type cubic structure with the unit cell parameter $a = 9.435$ Å (space group $P2_13$). Tl_9SbSe_6 has the Tl_5Te_3 type tetragonal crystal structure, space group $P4/n$, with the unit cell parameters $a = 8.539$ and $c = 12.69$ Å [22].

1.2.3. The section Tl_2Te–Sb_2Te_3

This section is characterized by formation of two intermediate ternary compounds $TlSbTe_2$ and Tl_9SbTe_6. The former decomposes by a peritectic reaction at 753 K, whereas the latter melts congruently at 798 K and forms a continuous solid solution field with Tl_2Te. The solubility in the solid phase based on Sb_2Te_3 was found to be about 5 mol% at 753 K. According to the literature [23], $TlSbTe_2$ has the hexagonal crystal structure of the $NaCrS_2$ type with the unit cell parameters $a = 4.425$ and $c = 23.303$ Å. Tl_9SbTe_6 is the

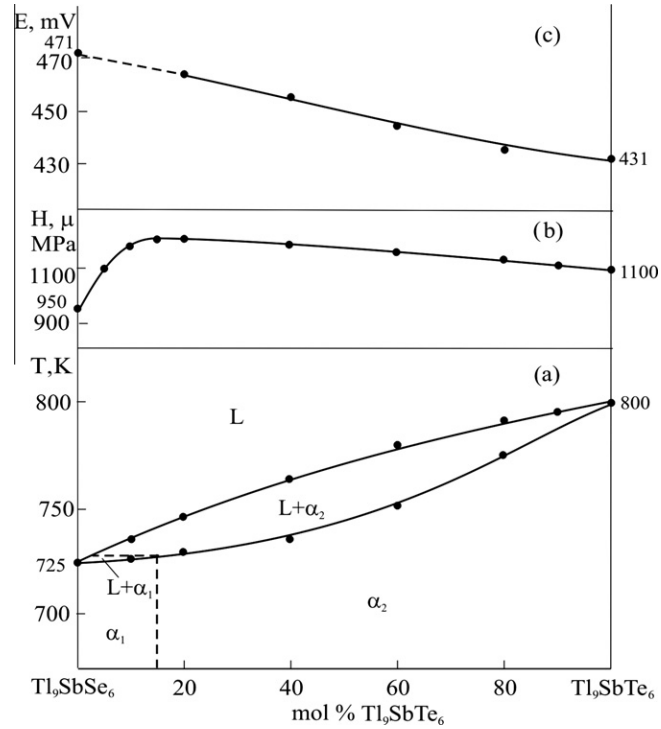

Fig. 2. Phase diagram (a), concentration relations of microhardnesses (b) and EMF of the chains of type (1) at 300 K (c) of the system Tl_9SbSe_6–Tl_9SbTe_6.

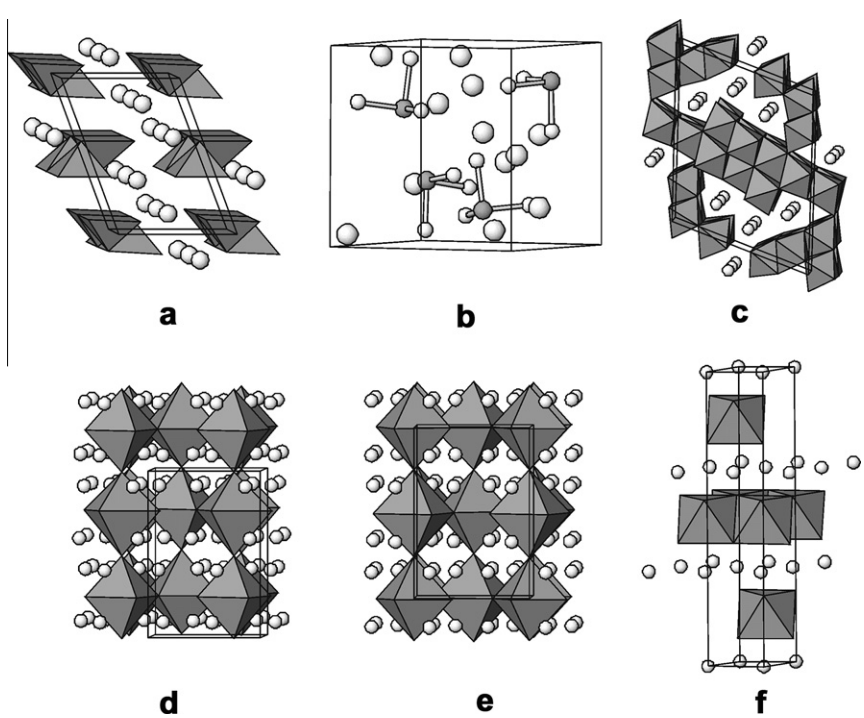

Fig. 1. Crystal structures of low-temperature $TlSbSe_2$ (a), Tl_3SbSe_3 (b), $TlSb_3Se_5$ (c), Tl_9SbTe_6 (d), Tl_9SbTe_6 (e), and $TlSbTe_2$ (f). Shown are polyhedra around antimony: square pyramids in (a), pyramids with Sb in a vertex (b), octaherda in all the rest. Thallium atoms are shown as large light spheres.

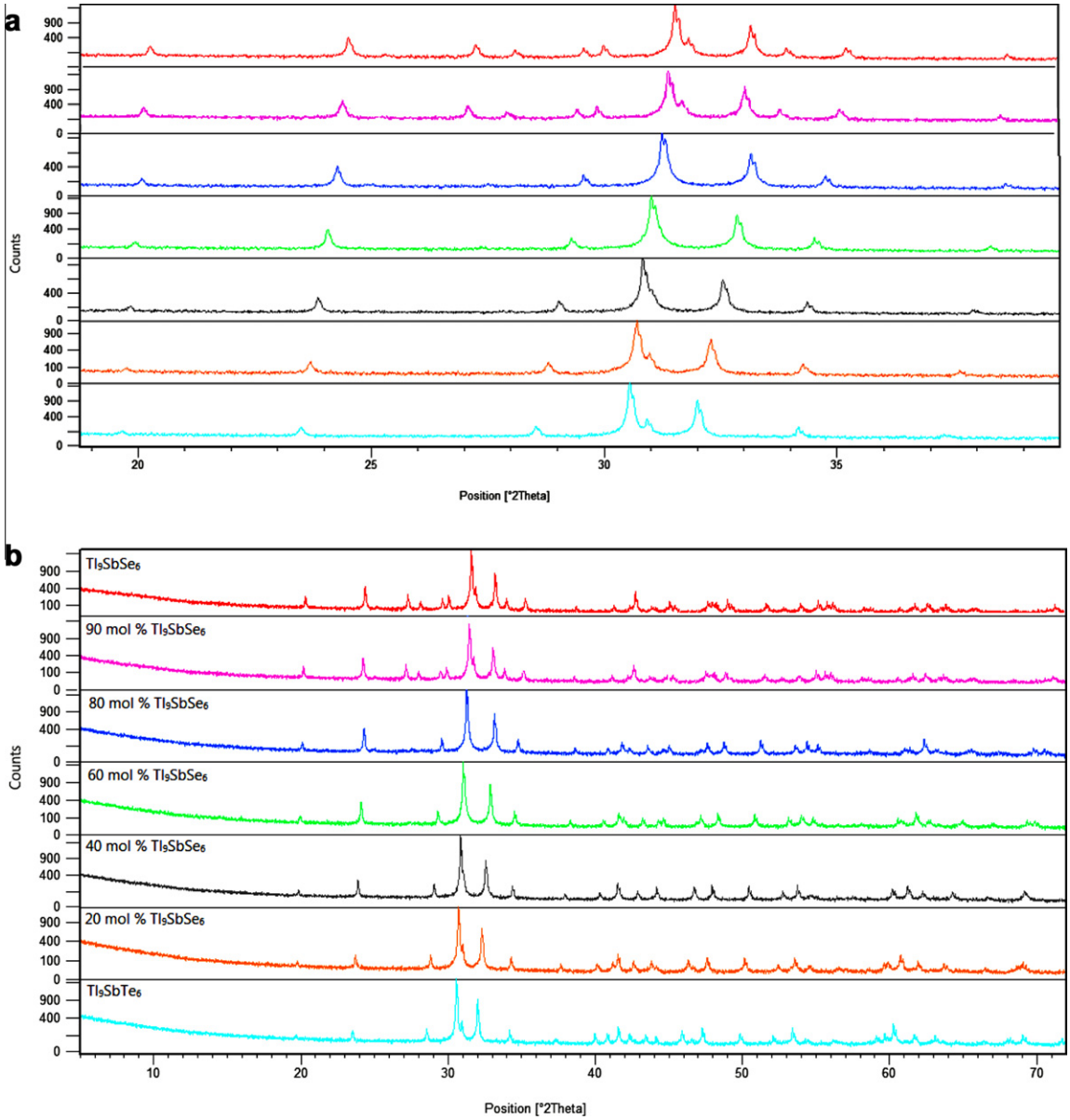

Fig. 3. XRD patterns for different compositions in the Tl_9SbSe_6–Tl_9SbTe_6 system: entire 2θ range (bottom), from 19° to 39° 2θ (top).

ternary analog of Tl_5Te_3 and has the tetragonal unit cell, space group $I4/m$, a = 8.828 Å and c = 13.001 Å [22,24].

1.2.4. The section Sb_2Se_3–Sb_2Te_3

This section is of eutectic type with limited solid solubility fields based on initial compounds [25]. The eutectic composition was found at 18 mol% Sb_2Te_3 and 833 K. The solid solubility based on Sb_2Te_3 and Sb_2Se_3 is achieved at 63 and 5 mol%, respectively, at room temperature.

Fig. 1 compiles the crystal structures of the above discussed ternary compounds.

2. Experimental

The starting binary Tl_2Se, Tl_2Te, Sb_2Se_3 and Sb_2Te_3 as well as ternary $TlSbSe_2$, $TlSbTe_2$, Tl_9SbSe_6, Tl_9SbTe_6, Tl_3SbSe_3, $TlSb_3Se_5$ compounds were synthesized by melting stoichiometric amounts of the respective high purity grade elements (not less than 99.999%) in evacuated ($\sim 10^{-2}$ Pa) sealed silica tubes. The quality of the synthesized compounds was checked by the differential thermal analysis (DTA) and X-ray diffraction analysis (XRD), which confirmed their purity. Alloys of the system (A) were prepared by melting the stoichiometric quantities of the pre-synthesized binary and ternary compounds in sealed silica tubes. After determining the corresponding solidus temperatures, all alloys were annealed at 20–50 K below the solidus for 800–1000 h in order to achieve complete homogenization.

XRD and DTA analyses and microhardness measurements were employed to analyze the samples. The XRD analysis was performed with a Bruker D8 ADVANCE diffractometer using the Cu-K_α radiation. DTA was performed using an NTR-74 device with two chromel–alumel thermocouples. Microhardness measurements were done with a microhardnesmeter PMT-3, the typical loading being 20 g. For the electro-motive force (EMF) measurements, the following concentration chains were used:

$$(-)\mathrm{Tl\ (solid)/glycerin + KCL + TlCl/Tl\ in\ alloys\ \ (solid)\ (+)} \quad (1)$$

In the chains of type (1), metallic thallium was the left (negative) electrode, while equilibrium alloys of the system (A) were exploited as the right (positive) electrode. A saturated glycerin solution of KCl with the addition of 1 mol% of TlCl was used as the electrolyte. The assembly of an electrochemical cell and measurements were similar to those reported elsewhere [26]. EMF was measured by the compensation method in the temperature range of 300–450 K using the high-resistance universal B7-34A digital voltmeter with the accuracy of ± 0.1 mV.

3. Results and discussion

The combined analysis of all our experimental data and the results found in the literature on the phase equilibria in the Tl_2Se–Tl_2Te [17], Tl_2Se–Sb_2Se_3 [18], Tl_2Te–Sb_2Te_3 [27,28] and Sb_2Se_3–Sb_2Te_3 [25] systems enabled us to construct the self-consistent diagram of the phase equilibriums in the mutual system (A).

3.1. Quasi-binary and partly quasi-binary sections

3.1.1. The section Tl_9SbSe_6–Tl_9SbTe_6

This is the only quasi-binary section of the system (A). According to the DTA results its phase diagram belongs to type I within the Roseboom's classification (Fig. 2a) though both initial compounds have different crystal structure. The XRD data shows (Fig. 3) that in the wide composition area (⩾15 mol% Tl_9SbTe_6) the solid solution has the Tl_9SbTe_6 type of the crystal structure, whereas the phase with 10 mol% Tl_9SbTe_6 is isostructural to Tl_9SbSe_6. The results of the microhardness measurements confirm that all samples contain just a single phase. The maximum values of microhardness are observed at 10–20 mol% Tl_9SbTe_6 (Fig. 2b).

Further confirmation of the XRD and microhardness analysis results comes from the EMF data. (Fig. 2c) clearly shows that the dependence of the EMF values on the composition is expressed by the monotonous curve that confirms continuous changes of the composition of the investigated phases, which are the right electrode of the chains of type (1).

Taking into account these results we assume that the heterogeneous region $\alpha_1 + \alpha_2$ degenerate nearest of the composition with 15 mol% Tl_9SbTe_6 and the $\alpha_1 \rightarrow \alpha_2$ phase transition can be considered as morphotropic. This can be explained by comparing the crystal structures of Tl_9SbSe_6 and Tl_9SbTe_6 (Fig. 1, panels d and e). Having almost the same metrics they differ slightly by the orientation of the $[SbE_6]$ octahedra (E = Se, Te) and a degree of displacement of the thallium atoms from their ideal positions.

3.1.2. The section $TlSbSe_2$–$TlSbTe_2$

This is the non quasi-binary section (Fig. 4) due to the incongruent character of $TlSbTe_2$, but it behaves as a quasi-binary system below 730 K. Liquidus consists of three parts corresponding to the primary crystallization of the γ_1', γ_2 and β_2-phase, which are the solid solutions based on the high-temperature modification of $TlSbSe_2$, $TlSbTe_2$ and Sb_2Te_3, respectively.

Below the liquidus curve of β_2-phase there is a curve corresponding to the secondary crystallization of the γ_2-phase, which occurs by a peritectic reaction $L + \beta_2 \rightarrow \gamma_2$. The eutectic contains approximately 17 mol% $TlSbTe_2$ and crystallizes at 710 K. The eutectoid point (E^*) lies at 635 K and 13 mol% $TlSbTe_2$. Wide solid solubility fields are formed in this system based on the initial ternary compounds.

The γ_1'-phase and γ_2-phase have maximum homogeneity fields at the temperature of eutectics with 13 and 80 mol%, respectively. The homogeneity field of the γ_1-phase based on low temperature modification of $TlSbSe_2$ has its maximum at the eutectoid temperature. The observed homogeneity fields of γ_1 and γ_2 at 400 K are achieved at about 10 and 76 mol%, respectively.

The results of the microhardness measurements confirmed the constructed phase diagram (Fig. 4b). Microhardness values of the solid solutions based on $TlSbSe_2$ and $TlSbTe_2$ increase monotonously upon increasing concentration of the second component, whereas in the two-phase area they remain constant.

The XRD data on the alloys air-quenched after annealing for about 600 h at 670 K are presented in Fig. 5. Apparently, the sample containing 90 mol% $TlSbSe_2$ displays a diffraction pattern that qualitatively similar to pure $TlSbSe_2$ whereas the alloys having

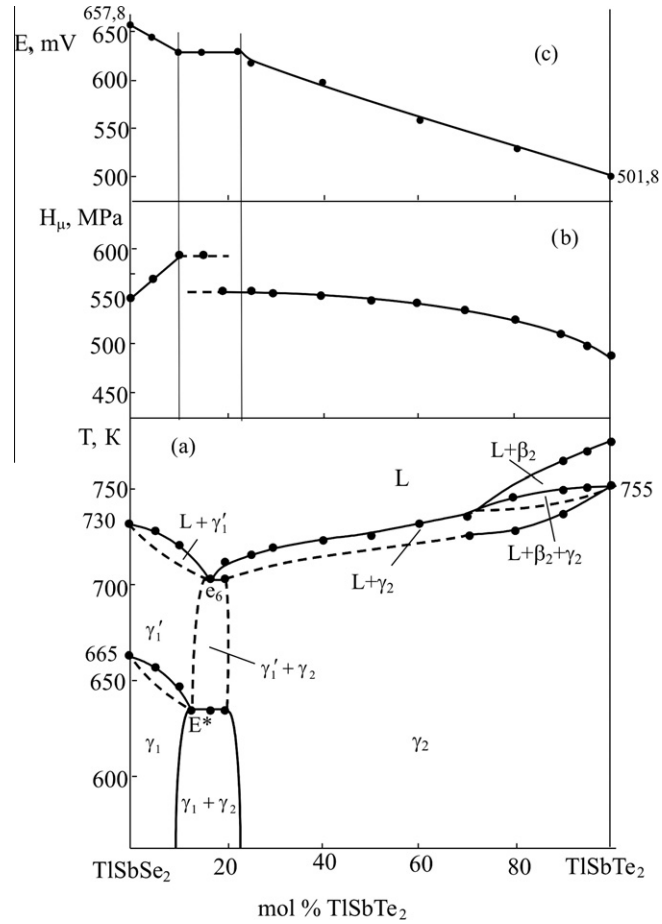

Fig. 4. Phase diagram (a), concentration relations of microhardnesses (b) and EMF of the chains of type (1) at 300 K (c) of the system $TlSbSe_2$–$TlSbTe_2$.

75, 50 and 20 mol% $TlSbSe_2$ are qualitatively similar to pure $TlSbTe_2$. Upon increasing the $TlSbSe_2$ content in alloys the corresponding peak positions are shifted towards higher angles. Combined, this confirms that the sample with 90 mol% $TlSbSe_2$ belongs to the solid solution based on $TlSbSe_2$, whereas the samples having 75, 50 and 20 mol% $TlSbSe_2$ are the solid solution based on $TlSbTe_2$. As can be seen in Fig. 5, the sample with 80 mol% $TlSbSe_2$ is the only two-phase alloy, and on the XRD pattern there are reflections from the γ_2-phase and the most intensive reflections of the γ_1'-phase.

The EMF measurements further confirm the phase diagram (Fig. 4c). Apparently, the EMF value is the linear function of the composition in the homogeneity fields of the γ_1 and γ_2-phases (with different increments), whereas in the two-phase area of $\gamma_1 + \gamma_2$ it remains constant independent of the relative content of the phases. The powder XRD patterns of the samples on the sections Tl_9SbSe_6–Tl_9SbTe_6 and $TlSbSe_2$–$TlSbTe_2$ were indexed by means of the TopasV3.0 software and the calculated unit cell parameters are listed in Table 1.

3.2. Solid-state phase equilibriums in the system (A)

The sections Tl_9SbSe_6–Tl_9SbTe_6 and $TlSbSe_2$–$TlSbTe_2$ divide the system (A) into three independent subsystems: Tl_2Se–Tl_2Te–Tl_9SbTe_6–Tl_9SbSe_6, Tl_9SbSe_6–Tl_9SbTe_6–$TlSbTe_2$–$TlSbSe_2$ and $TlSbSe_2$–$TlSbTe_2$–Sb_2Te_3–Sb_2Se_3 (Fig. 6).

The first subsystem is fully covered by the fields of the solid solutions with the Tl_2Se (α_1), Tl_9SbTe_6 (α_2) and Tl_2Te (α_3) structure types. The borders of the α_1 and α_2 phases as well as two-phase

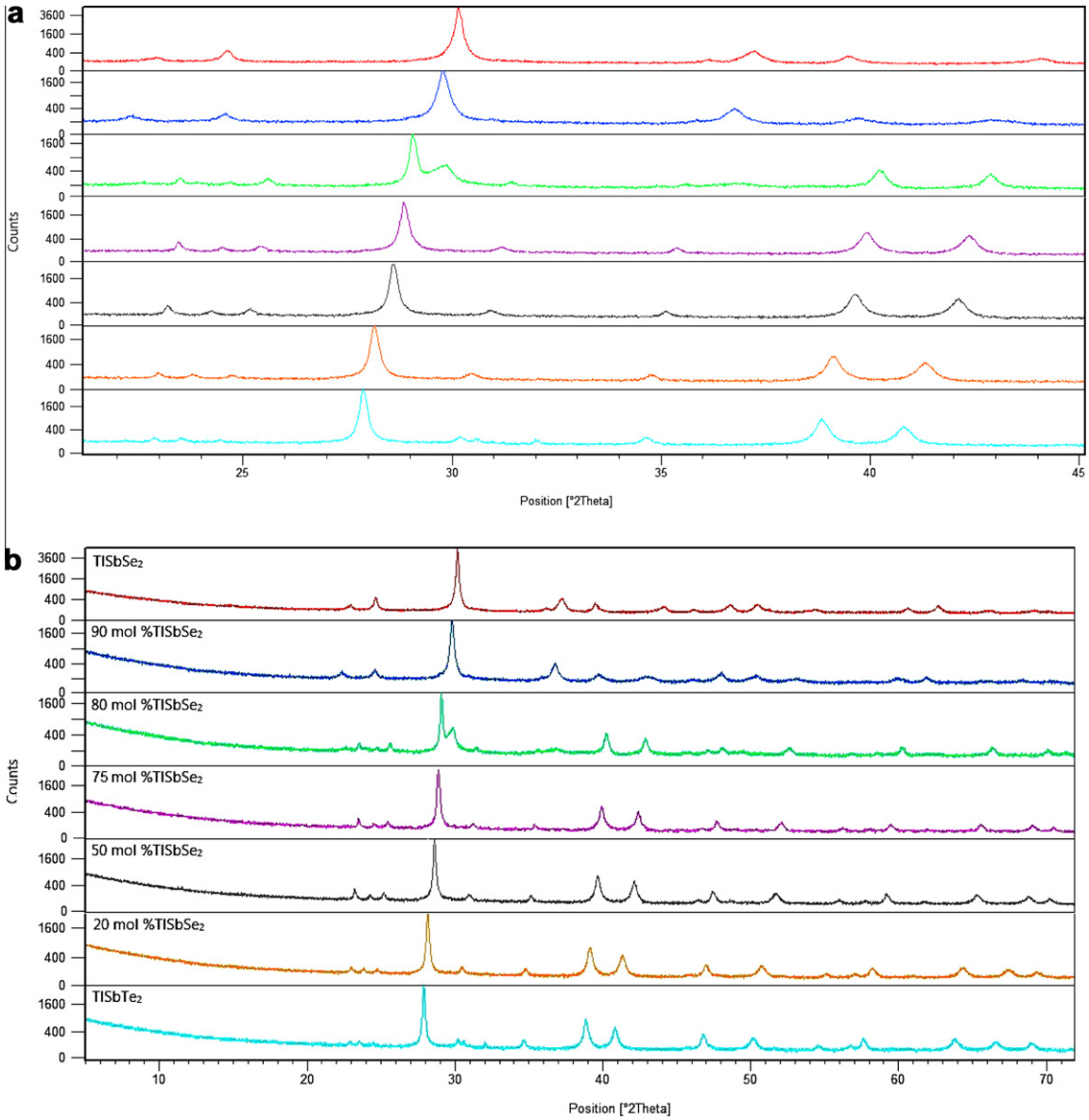

Fig. 5. XRD patterns for different compositions in the $TlSbSe_2$–$TlSbTe_2$ system: entire 2θ range (bottom), from 21° to 45° 2θ (top).

Table 1
Crystal structure parameters of the solid solutions in the $TlSbSe_2$–$TlSbTe_2$ and Tl_9SbSe_6–Tl_9SbTe_6 subsystems.

Section	Composition	Crystal system	Lattice parameters, Å		
			a	b	c
$TlSbSe_2$–$TlSbTe_2$	$TlSbSe_2$	Orthorhombic	11.9146(5)	4.145(2)	4.5414(14)
	$TlSbSe_{1.8}Te_{0.2}$	Orthorhombic	12.009(3)	4.213(1)	4.5409(11)
	$TlSbSe_{1.5}Te_{0.5}$	Rhombohedral	4.2195(3)		22.716(2)
	TlSbSeTe	Rhombohedral	4.2117(7)		22.709(2)
	$TlSbSe_{0.4}Te_{1.6}$	Rhombohedral	4.3695(15)		23.211(4)
	$TlSbTe_2$	Rhombohedral	4.3372(9)		23.324(4)
Tl_9SbSe_6–Tl_9SbTe_6	Tl_9SbSe_6	Tetragonal	8.5334(2)		12.6944(3)
	$Tl_9SbSe_{5.4}Te_{0.6}$	Tetragonal	8.5347(1)		12.7741(3)
	$Tl_9SbSe_{4.8}Te_{1.2}$	Tetragonal	8.5365(1)		12.9509(3)
	$Tl_9SbSe_{3.6}Te_{2.4}$	Tetragonal	8.6923(3)		13.0157(3)
	$Tl_9SbSe_{2.4}Te_{3.6}$	Tetragonal	8.7639(2)		13.0217(8)
	$Tl_9SbSe_{1.2}Te_{4.8}$	Tetragonal	8.8352(1)		13.0434(4)
	Tl_9SbTe_6	Tetragonal	8.8352(1)		13.0270(2)

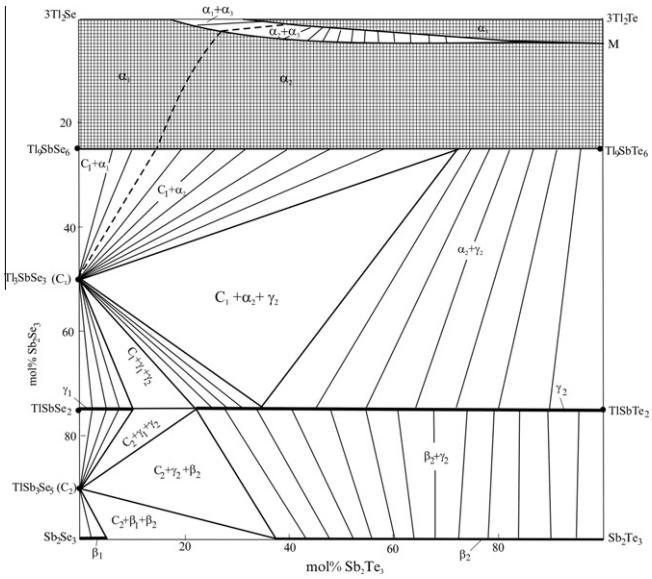

Fig. 6. Isothermal section at 300 K of the phase diagram of the $3Tl_2Se + Sb_2Te_3$ ↔$3Tl_2Te + Sb_2Se_3$ mutual system.

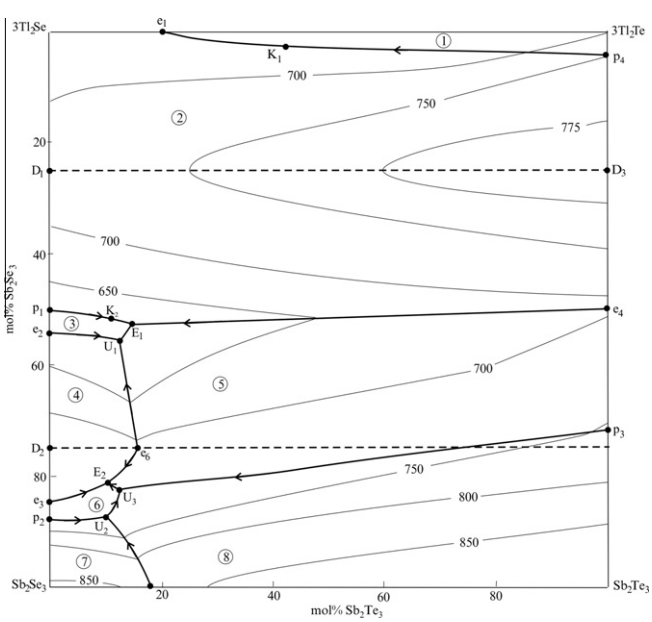

Fig. 7. Projection of the liquidus surface of the $3Tl_2Se + Sb_2Te_3 3Tl_2Te + Sb_2Se_3$ system. Primary crystallization fields are shown: 1, α_3; 2, α_1 (α_2); 3, Tl_3SbSe_3 (C_1); 4, γ_1' (γ_1); 5, γ_2; 6, $TlSb_3Se_5$ (C_2); 7, β_1; 8, β_2.

regions of $C_1 + \alpha_1$ and $C_1 + \alpha_2$ are shown by dashed lines in Fig. 6. The two-phase area $\alpha_1 + \alpha_2$ is degenerated, whereas the $\alpha_2 + \alpha_3$ area is continuously narrowed with increasing the tellurium content and practically degenerated at the M point (Fig. 6).

Two other subsystems consist of different two- and three-phase regions formed from various combinations of the α_1, α_2, α_3, β_1, β_2, γ_1 and γ_2-phases as well as ternary compounds Tl_3SbSe_3 (C_1) and $TlSb_3Se_5$ (C_2). The borders of these regions were determined by means of analyzing the XRD patterns and from the comparison of the DTA results for certain polythermal sections.

3.3. The liquidus surface of the system (A)

The liquidus surface of the system (A) (Fig. 7) consists of eight fields corresponding to primary crystallization of various phases.

Table 2
Invariant equilibriums in the $3Tl_2Se + Sb_2Te_3 3Tl_2Te + Sb_2Se_3$ system.

Point in Fig. 7	Equilibrium	Composition, mol%			t, K
		$3Tl_2Se$	$3Tl_2Te$	Sb_2Se_3	
D_1	$L \leftrightarrow Tl_9SbSe_6$	75		25	725
D_2	$L \leftrightarrow TlSbSe_2$	25		75	730
D_3	$L \leftrightarrow Tl_9SbTe_6$		75		798
e_1	$L \leftrightarrow \alpha_1 + \alpha_3$	80	20		648
e_2	$L \leftrightarrow Tl_3SbSe_3 + \gamma_1$	46		54	610
e_3	$L \leftrightarrow TlSb_3Se_5 + \gamma_1'$	17		83	705
e_4	$L \leftrightarrow \alpha_2 + \gamma_2$		50		685
e_5	$L \leftrightarrow \beta_1 + \beta_2$			82	833
e_6	$L \leftrightarrow \gamma_1' + \gamma_2$	8	17	75	710
p_1	$L + \alpha_1 \leftrightarrow Tl_3SbSe_3$	49		51	625
p_2	$L + \beta_1 \leftrightarrow TlSb_3Se_5$	13		87	740
p_3	$L + \beta_2 \leftrightarrow \gamma_2$		28		753
p_4	$L + \alpha_2 \leftrightarrow \alpha_3$		97		700
U_1	$L + \gamma_1 \leftrightarrow Tl_3SbSe_3 + \gamma_2$	29	13	58	605
U_2	$L + \beta_1 \leftrightarrow TlSb_3Se_5 + \beta_2$	3	10	87	705
U_3	$L + \beta_2 \leftrightarrow TlSb_3Se_5 + \gamma_2$	5	13	82	690
E_1	$L \leftrightarrow Tl_3SbSe_3 + \alpha_2 + \gamma_2$	30	15	55	600
E_2	$L \leftrightarrow TlSb_3Se_5 + \gamma_1 + \gamma_2$	8	11	81	685

Table 3
Monovariant equilibriums in the $3Tl_2Se + Sb_2Te_3 \leftrightarrow 3Tl_2Te + Sb_2Se_3$ system.

Curve in Fig. 7	Equilibrium	Temperature interval, K
p_4K_1	$L + \alpha_2 \leftrightarrow \alpha_3$	700–660
K_1e_1	$L \leftrightarrow \alpha_3 + \alpha_1(\alpha_2)$	660–648
p_1K_2	$L + \alpha_1(\alpha_2) \leftrightarrow Tl_3SbSe_3$	625–610
K_2E_1	$L \leftrightarrow \alpha_2 + Tl_3SbSe_3$	610–600
e_2U_1	$L \leftrightarrow \gamma_1 + Tl_3SbSe_3$	610–605
U_1E_1	$L \leftrightarrow \gamma_2 + Tl_3SbSe_3$	605–600
e_6U_1	$L \leftrightarrow \gamma_1 + \gamma_2$	710–605
e_6E_2	$L \leftrightarrow \gamma_1\gamma_2$	710–685
e_3E_2	$L \leftrightarrow \gamma_1 + TlSb_3Se_5$	705–685
p_2U_2	$L + \beta_1 \leftrightarrow TlSb_3Se_5$	740–705
e_5U_2	$L \leftrightarrow \beta_1 + \beta_2$	833–705
U_2U_3	$L \leftrightarrow \beta_2 + TlSb_3Se_5$	705–690
U_3E_2	$L \leftrightarrow \gamma_2 + TlSb_3Se_5$	690–685
e_4E_1	$L \leftrightarrow \alpha_2 + \gamma_2$	685–600
p_3U_3	$L + \beta_2 \leftrightarrow \gamma_2$	753–690

We were unable to accurately differentiate the fields of primary crystallization of the α_1 and α_2 phases. They together occupy a very wide area in Fig. 6. The primary crystallization fields of the β_2 and γ_2 phases are also having a wide extension, which allows the variety of the compositions of alloys for growing of single crystals of the solid solutions.

Table 2 summarizes the types and coordinates of nonvariant equilibriums, including border systems, whereas Table 3 compiles the types and temperature intervals for the monovariant equilibriums. The interesting feature of the given system is the transitions of two peritectic equilibriums into the corresponding eutectics (Fig. 7, Table 3). The approximate points of these transitions (K_1 and K_2) are labeled on the p_4e_1 and p_1E_1 curves.

3.4. Several polythermal sections of the phase diagram of the system (A)

In order to achieve the self-consistent phase diagram of the system (A), we studied the polythermal sections $3Tl_2Se$–Sb_2Te_3, $3Tl_2Te$–Sb_2Se_3, $2Tl_2Se$–$TlSbTe_2$, $2Tl_2Te$–$TlSbSe_2$, $1.5TlSbTe_2$–Sb_2Se_3 and $1.5TlSbSe_2$–Sb_2Te_3 as well as a number of samples which compositions positioned out of these sections. Below, the diagonal sections 3Tl2Se–Sb_2Te_3 and $3Tl_2Te$–Sb_2Se_3 are discussed and are

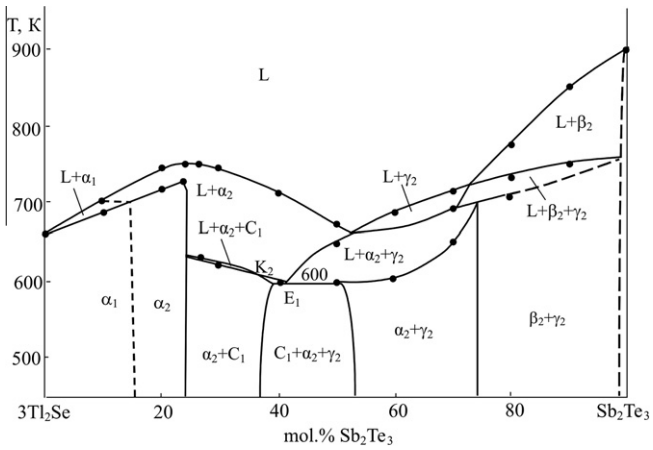

Fig. 8. Polythermal section $3Tl_2Se–Sb_2Te_3$ of the $3Tl_2Se + Sb_2Te_3 3Tl_2Te + Sb_2Se_3$ phase diagram.

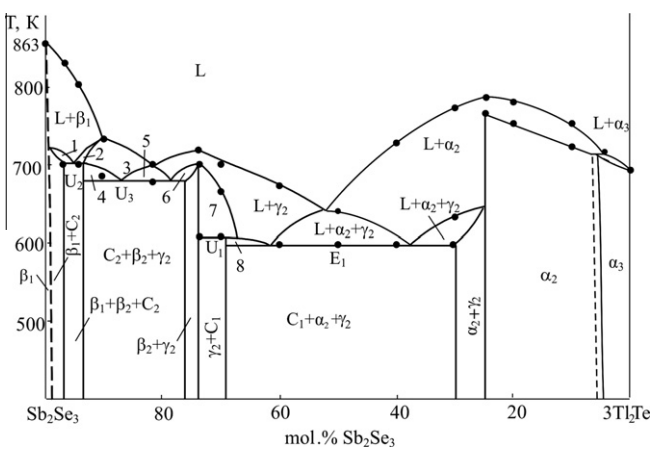

Fig. 9. Polythermal section $3Tl_2Te–Sb_2Se_3$ of the $3Tl_2Se + Sb_2Te_3 3Tl_2Te + Sb_2Se_3$ phase diagram. Phase areas: 1, L + β_1 + C_2; 2, L + β_1 + β_2; 3, L + β_2; 4, L + C_2 + β_2; 5, 6, L + β_2 + γ_2; 7, L + γ_1 + γ_2, 8, L + C_1 + γ_2.

compared with the general T-x-y diagram of the quaternary mutual system.

3.4.1. The section $3Tl_2Se–Sb_2Te_3$

This section (Fig. 8) crosses the primary crystallization field of the α_1, α_2, γ_2 and β_2 phases. In the composition range of 0–25 mol% Sb_2Te_3 the liquid phase completely crystallizes to form pure α_1-phase or α_2-phase. The border of these phases is found to have the composition corresponding to $\sim$ 16 mol% Sb_2Te_3.

After primary crystallization of the β_2-phase from the melt containing more than 75 mol% Sb_2Te_3, the $TlSbTe_2$ based γ_2-phase crystallizes by the monovariant peritectic reaction (Table 3, the curve p_3U_3) and forms the two-phase field $\gamma_2 + \beta_2$.

In the composition range of 25–40 mol% Sb_2Te_3, after primary crystallization of α_2-phase, observed is the formation of Tl_3SbSe_3 by the monovariant peritectic reaction (Table 3, Fig. 7, the curve p_1K_2), the latter transforms into a eutectic equilibrium (the curve K_2E_1) nearest of E_1.

In the region of 40–75 mol% Sb_2Te_3, crystallization of the two-phase mixture $\alpha_2 + \gamma_2$ occurs. The crystallization process finishes with the quadriphase eutectic reaction (E_1) in the region of 40–50 mol% Sb_2Te_3.

3.4.2. The section $3Tl_2Te–Sb_2Se_3$

This section (Fig. 9) is characterized by a complex reaction pattern. It intersects four single-phase (β_1, γ_2, α_2, α_3), five two-phase ($\beta_1 + C_2$, $\beta_2 + \gamma_2$, $\gamma_2 + C_1$, $\alpha_2 + \gamma_2$, $\alpha_2 + \alpha_3$) and three three-phase ($\beta_1 + \beta_2 + C_2$, $\beta_2 + \gamma_2 + C_2$, $C_1 + \alpha_2 + \gamma_2$) fields in the subsolidus area. Concentration and temperature ranges of primary crystallization of phases and monovariant equilibriums are in good agreement with Fig. 7.

This section clearly features four horizontals lines at 705, 690, 605 and 600 K, respectively, according to invariant transition (U_2, U_3, U_1) and eutectic (E_1) equilibriums (Table 2).

3.5. Thermodynamic properties of the solid solutions

The results of the EMF measurements of the chains of type (1) allowed calculating thermodynamic properties of alloys of the sections $Tl_9SbSe_6–Tl_9SbTe_6$ and $TlSbSe_2–TlSbTe_2$. The analysis showed the linearity of the EMF dependences upon temperature for all alloys. Accordingly, the linear least-square treatment of the data was performed [26] and the results were expressed according to the literature recommendations [29] as:

$$E = a + bT \pm t\left[\frac{S_E^2}{n} + S_b^2(T - \overline{T})^2\right]^{1/2} \quad (2)$$

where n is the number of pairs of E and T values; S_E and S_b are the error variances of the EMF readings and b coefficient, respectively; $\overline{T}$ is the average of the absolute temperature; t is the Student's test. At the confidence level of 95% and $n \geqslant 20$, the Student's test is $t \leqslant 2$ [26]. The composed equation of the mode (2) is presented in Table 4.

The partial molar functions of thallium ($\Delta\bar{G}, \Delta\bar{H}, \Delta\bar{S}$) (Table 5) in the α_2, γ_1 and γ_2- phase, as well as in $\gamma_1 + \gamma_2$ two-phase alloys were calculated by known thermodynamic relations [26] taking into account the phase state of alloys by using data from the Table 4. The graphical dependences of the partial molar functions of thallium of the composition for the sections $Tl_9SbSe_6–Tl_9SbTe_6$ and $TlSbSe_2–TlSbTe_2$ are plotted based on Table 5 (Fig. 10a and b). As can be seen from Fig. 10, the isotherms of $\Delta\bar{G}_{Tl}$, $\Delta\bar{H}_{Tl}$ and $\Delta\bar{S}_{Tl}$ are continuous and monotonous functions of the composition in the homogonous range of the γ_1 and γ_2 phases. In the two-phase region $\gamma_1 + \gamma_2$ their values remain constant regardless of the common composition, which is due to the constant composition of both phases in this area.

It should be noted that the monotonous character of the concentration dependences of the partial thermodynamic functions of thallium in the homogeneity regions of the α_2, γ_1 and γ_2 phases indicates that formation of the solid solutions in the systems $Tl_9SbSe_6–Tl_9SbTe_6$ and $TlSbSe_2–TlSbTe_2$ is accompanied by minor structural and energetic changes. Besides, it confirms that the α_2, γ_1 and γ_2 phases belong to the substitutional type of solid solutions.

4. Conclusions

We have shown that $Tl_2Se + Sb_2Te_3 \leftrightarrow Tl_2Te + Sb_2Se_3$ is a mutual quaternary system that features wide solubility fields along the $TlSbSe_2–TlSbTe_2$ non quasi-binary section and within the $Tl_2Se–Tl_9SbSe_6–Tl_9SbTe_6–Tl_2Te$ subsystem. The only quasi-binary section $Tl_9SbSe_6–Tl_9SbTe_6$ shows a morphotropic phase transition between the solid solutions based on the Se and Te derivatives. The liquidus surface of the system consists of eight fields occupying very wide compositional area. The calculated partial molar thermodynamic functions of thallium prove that the formation of the solid solutions is accompanied by minor energetic changes, reflecting minor

Table 4
Temperature dependencies of the EMF for the chains of type (1) in the $TlSbSe_2$–$TlSbTe_2$ and Tl_9SbSe_6–Tl_9SbTe_6 system (T = 300–430 K).

	Phase area, mol% $TlSbTe_2$ (Tl_9SbTe_6)	$E, mV = a + bT \pm t\left[\frac{S_E^2}{n} + S_b^2(T-\overline{T})^2\right]^{1/2}$
$TlSbSe_2$–$TlSbTe_2$	0 ($TlSbSe_2$) [25]	$685,1 - 0,091T \pm 2\left[\frac{33,4}{40} + 5\cdot 10^{-4}(T-366,4)^2\right]^{1/2}$
	5 (γ_1)	$661,7 - 0,074T \pm 2\left[\frac{5,6}{28} + 7\cdot 10^{-4}(T-367,2)^2\right]^{1/2}$
	10–24 (γ_1+ γ_2)	$638,7 - 0,046T \pm 2\left[\frac{4,8}{28} + 6\cdot 10^{-4}(T-367,2)^2\right]^{1/2}$
	25 (γ_2)	$620,2 - 0,017T \pm 2\left[\frac{4,2}{28} + 5\cdot 10^{-4}(T-367,2)^2\right]^{1/2}$
	40 (γ_2)	$580,2 + 0,032T \pm 2\left[\frac{5,4}{28} + 4\cdot 10^{-4}(T-367,2)^2\right]^{1/2}$
	60 (γ_2)	$533,6 + 0,084T \pm 2\left[\frac{3,6}{28} + 2\cdot 10^{-5}(T-367,2)^2\right]^{1/2}$
	80 (γ_2)	$489,7 + 0,134T \pm 2\left[\frac{5,2}{28} + 4\cdot 10^{-4}(T-367,2)^2\right]^{1/2}$
	100 ($TlSbTe_2$) [25]	$468,8 + 0,111T \pm 2\left[\frac{4,7}{40} + 7\cdot 10^{-4}(T-368,6)^2\right]^{1/2}$
Tl_9SbSe_6–Tl_9SbTe_6	0 (Tl_9SbSe_6) [25]	$486,2 - 0,052T \pm 2\left[\frac{22,5}{40} + 0,0003(\mathrm{T}-366,5)^2\right]^{1/2}$
	20(α_2)	$468,7 - 0,018T \pm 2\left[\frac{1,3}{20} + 4\cdot 10^{-5}(\mathrm{T}-368,4)^2\right]^{1/2}$
	40(α_2)	$450,4 + 0,016T \pm 2\left[\frac{1,8}{20} + 1,3\cdot 10^{-4}(\mathrm{T}-368,4)^2\right]^{1/2}$
	60(α_2)	$426,4 + 0,058T \pm 2\left[\frac{1,1}{20} + 3\cdot 10^{-5}(\mathrm{T}-368,4)^2\right]^{1/2}$
	80(α_2)	$405,9 + 0,097T \pm 2\left[\frac{2,4}{20} + 1,8\cdot 10^{-4}(\mathrm{T}-368,4)^2\right]^{1/2}$
	100 (Tl_9SbTe_6) [25]	$402,7 + 0,094T \pm 2\left[\frac{34,7}{40} + 5\cdot 10^{-4}(\mathrm{T}-367,8)^2\right]^{1/2}$

Table 5
Relative partial thermodynamic functions of thallium in the solid solutions of the $TlSbSe_2$–$TlSbTe_2$ and Tl_9SbSe_6–Tl_9SbTe_6 systems at 298 K.

Section	Composition mol% $TlSbTe_2$ (Tl_9SbTe_6)	$-\Delta\bar{G}_{Tl}$	$-\Delta\bar{H}_{Tl}$	$\Delta\bar{S}_{Tl}$
		(kJ mol^{-1})		(J·K^{-1} mol^{-1})
$TlSbSe_2$–$TlSbTe_2$	0 ($TlSbSe_2$) [25]	63,49 ± 0,34	66,10 ± 1,59	−8,8 ± 4,31
	5 (γ_1)	61,72 ± 0,36	63,85 ± 1,88	−7,1 ± 5,1
	10–24 (γ_1+ γ_2)	60,30 ± 0,34	61,63 ± 1,74	−4,4 ± 4,7
	25 (γ_2)	59,35 ± 0,31	55,98 ± 1,59	−1,6 ± 4,3
	40 (γ_2)	56,90 ± 0,28	55,98 ± 1,42	3,1 ± 3,9
	60 (γ_2)	53,90 ± 0,20	51,49 ± 1,00	8,1 ± 2,7
	80 (γ_2)	51,10 ± 0,28	47,25 ± 1,42	12,9 ± 3,9
	100 ($TlSbTe_2$) [25]	48,42 ± 0,35	45,23 ± 1,89	10,7 ± 5,1
Tl_9SbSe_6–Tl_9SbTe_6	0 (Tl_9SbSe_6) [25]	45,42 ± 0,27	46,91 ± 1,20	−5,0 ± 3,4
	20(α_2)	44,71 ± 0,10	45,2 ± 0,45	−1,7 ± 1,2
	40(α_2)	43,92 ± 0,17	43,46 ± 0,81	1,5 ± 2,2
	60(α_2)	42,81 ± 0,40	41,14 ± 0,39	5,6 ± 1,1
	80(α_2)	41,95 ± 0,19	39,16 ± 0,96	9,4 ± 2,7
	100(Tl_9SbTe_6) [25]	41,56 ± 0,35	38,85 ± 1,60	9,1 ± 4,3

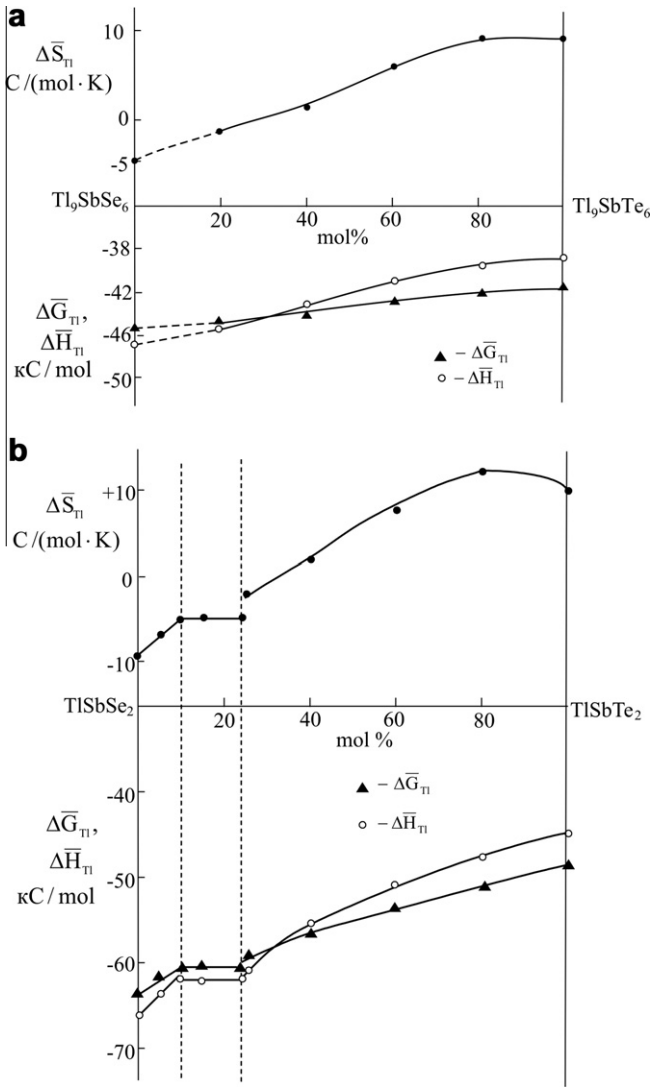

Fig. 10. Dependence of the relative partial thermodynamic functions of thallium on the composition in the Tl_9SbSe_6–Tl_9SbTe_6 (a) and $TlSbSe_2$–$TlSbTe_2$ (b) systems.

structural changes upon forming such solid solutions of substitution type.

Acknowledgment

This work was supported by Science Development Foundation under the President of the Republic of Azerbaijan, grant no EIF-2011-1(3)-82/69/4-M-50.

References

[1] A.V. Shevelkov, Russ. Chem. Rev. 77 (2008) 1–19; Uspekhi Khimii 77 (2008) 3–21.
[2] M.G. Kanatzidis, Acc. Chem. Res. 38 (2005) 361–370.
[3] M.A. McGuire, T.K. Reynolds, F.J. DiSalvo, Chem. Mater. 17 (2005) 2875–2884.
[4] S.V. Eremeev, G. Landolt, T.V. Menshchikova, B. Slomski, Yu.M. Koroteev, Z.S. Aliev, M.B. Babanly, J. Henk, A. Ernst, L. Patthey, A. Eich, A.A. Khajetoorians, J. Hagemeister, O. Pietzsch, J. Wiebe, R. Wiesendanger, P.M. Echenique, S.S. Tsirkin, I.R. Amiraslanov, J.H. Dil, E.V. Chulkov, Nat. Commun. 3 (2012) 635.
[5] S.V. Eremeev, Y.M. Koroteev, E.V. Chulkov, JETP Lett. 91 (2010) 664–668.
[6] Y.I. Jafarov, M.B. Babanly, Inorg. Mater. 54 (2009) 1920–1924.
[7] M.B. Babanly, S.M. Veisova, Z.A. Huseynov, Russ. J. Inorg. Chem. 47 (2002) 1020–1025.
[8] S.M. Veisova, Z.A. Huseynov, F.N. Huseynov, M.B. Babanly, Ser. Nat. Sci. 3 (2004) 10–20.
[9] Y.I. Jafarov, A.M. Mirzoeva, M.B. Babanly, Russ. J. Inorg. Chem. 53 (2008) 146–152.
[10] Y.I. Jafarov, A.M. Mirzoeva, M.B. Babanly, Russ. J. Inorg. Chem. 51 (2006) 871–875.
[11] Y.I. Jafarov, N.A. Rzaeva, M.B. Babanly, Inorg. Mater. 44 (2008) 1314–1318.
[12] M.B. Babanly, S.M. Veisova, Z.A. Huseynov, Y.A. Yusibov, Russ. J. Inorg. Chem. 48 (2003) 1562–1568.
[13] , second ed.T.B. Massalski (Ed.), Binary Alloy Phase Diagrams, ASM International, Materials park, Ohio, 1990, p. 3875.
[14] N.P. Lyakishev (Ed.), Handbook of The Phase Diagrams of Binary Metallic Systems, vols. 1-2, Masinostroyenie Publ., Moscow, 1996.
[15] A.V. Novoselova, V.B. Lazarev (Eds.), Handbook of Physico-Chemical Properties of Semiconductor Materials, Nauka Publ., Moscow, 1976, p. 339.
[16] R. Cerny, J. Joubert, Y. Filinchuk, Y. Feutelais, Acta Crystallogr. C. 58 (2002) 163–166.
[17] M.M. Asadov, M.B. Babanly, A.A. Kuliev, Az. Chem. J. 2 (1977) 94–95.
[18] Y.I. Jafarov, M.B. Babanly, A.A. Kuliev, Russ. J. Inorg. Chem. 43 (1998) 779–781.
[19] R. Wacker, M. Salk, G. Decker-Schultheiss, F. Keeler, Z. Anorg. Allg. Chem. 606 (1991) 51–58.
[20] R. Wacker, P. Buck, Mater. Res. Bull. 15 (1989) 1105–1112.
[21] .A. Olsen, P. Goodman, H.J. Whitfield, J. Solid State Chem. 60 (1985) 305–315.
[22] K. Wacker, Z. Kristallogr. Suppl. 3 (1991) 281.
[23] E.F. Hockings, J.G. White, Acta Crystallogr. 14 (1961) 328–329.
[24] P. Böttcher, T. Doert, C. Druska, S. Bradtmöller, J. Alloys Comp. 246 (1997) 209–215.
[25] V.I. Ivlieva, N.X. Abrikosov, Dokl. Chem. 159 (1964) 1326–1329.
[26] M.B. Babanly, Y.A. Yusibov, Electrochemical Methods in Thermodynamics of Inorganic Systems. Baku, 2011, 306p. (ISBN 978-9952-453-17-1).
[27] I.V. Botgros, K.R. Zbigli, A.V. Stanchu, G.I. Stepanov, G.D. Chumak, Inorg. Mater. 13 (1977) 1202–1206.
[28] M.B. Babanly, A. Azizulla, A.A. Kuliev, Russ. J. Inorg. Chem. 30 (1985) 1051–1059.
[29] A.N. Kornilov, J. Phys. Chem. 41 (1967) 3096–3101.